Chemical
Science

ROYAL SOCIETY
OF CHEMISTRY

EDGE ARTICLE

View Article Online
View Journal | View Issue

Check for updates

Cite this: *Chem. Sci.*, 2025, **16**, 17827

All publication charges for this article have been paid for by the Royal Society of Chemistry

Received 24th June 2025
Accepted 26th August 2025

DOI: 10.1039/d5sc04639d

rsc.li/chemical-science

A dual-engineered covalent organic framework with charge-oxygen synergy promotes photocatalytic dipolar [3 + 2] cycloaddition

Yuemeng Liu,[a] Lifan Shen,[a] Hao Yang,[a] Xiaojia Zhao[b] and Xingwang Lan*[a]

The photocatalytic oxidative dipolar [3 + 2] cycloaddition reaction is a promising green approach for producing pyrrolo[2,1-*a*]isoquinolines. However, developing sustainable cycloaddition methods with heterogeneous photocatalysts is still in its infancy, largely owing to their low reactivity and photostability. Herein, we propose a charge–oxygen synergy strategy through a dual-engineered covalent organic framework (COF) by integrating π-spacers with donor–acceptor motifs to promote intermolecular cycloaddition. Systematic analyses reveal that electron-deficient thiadiazole units significantly enhance exciton dissociation efficiency, while a fully conjugated acetenyl spacer promotes spontaneous oxygen adsorption to stabilize endoperoxide intermediate species. This synergistic interplay between charge separation and oxygen activation significantly boosts reactive oxygen species generation, enabling efficient C–H bond activation under visible light. Remarkably, the BTDE-COF efficiently promotes dipolar [3 + 2] cycloaddition, achieving up to 97.1% yield with a broad substrate scope under visible light irradiation, while enabling a gram-scale synthesis. This work suggests that strategically engineering COFs has the potential to foster a variety of visible light-mediated energy-transfer processes.

Introduction

Pyrrolo[2,1-*a*]isoquinoline scaffolds, consisting of a pyrrole ring fused with an isoquinoline system, are important structural motifs found in alkaloids and pharmaceutical molecules,[1–3] exhibiting promising bioactivities including antitumor properties, antibiotic effects, HIV-1 integrase inhibition, and reversal of multidrug resistance in cancer therapy[4] (Scheme 1a). Therefore, various synthetic methods have been constantly developed to construct pyrrolo[2,1-*a*]isoquinoline cores, including 1,3-dipolar cycloaddition,[5] multicomponent reaction pathway,[6] oxidative dimerization,[7] and so on. Among the existing strategies, the 1,3-dipolar [3 + 2] cycloaddition reaction represents a particularly appealing and straightforward approach for the construction of pyrrolo[2,1-*a*]isoquinoline due to its ability to form two new C–C bonds in a single step (Scheme 1b). This approach has garnered significant attention and has been extensively explored using various catalytic systems, including metal complexes and molecular catalysts with suitable oxidants.[8] With the rapid development of visible light photocatalysis, photocatalytic oxidative reactions utilizing molecular oxygen can serve as an efficient avenue for dipolar cycloaddition. However, the photocatalytic systems employed thus far have predominantly relied on homogeneous molecular photocatalysts, such as [Ru(bpy)$_3$]Cl$_2$, Bodipy species, Rose Bengal, or methylene blue.[9–12] These catalysts exhibited high efficiency, but they are usually homogeneous. While these catalysts demonstrate high efficiency, their homogeneous nature poses challenges in terms of recovery and reuse. Consequently, the development of innovative metal-free heterogeneous photocatalysts for photocatalytic oxidative dipolar [3 + 2] cycloaddition reactions is highly desirable.

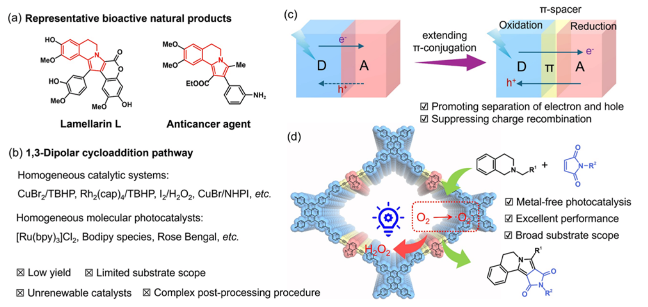

Scheme 1 (a) Representative bioactive natural products. (b) 1,3-Dipolar cycloaddition pathway over different catalytic systems. (c) Extending the π-conjugation system for the D–A system. (d) The photocatalytic oxidative cycloaddition pathway for the synthesis over BTDE-COF.

---

[a] *College of Chemistry and Materials Science, Key Laboratory of Chemical Biology of Hebei Province, Hebei Research Center of the Basic Discipline of Synthetic Chemistry, Institute of Life Science and Green Development Hebei University Baoding, Hebei, 071002, P. R. China. E-mail: lanxingwang@hbu.edu.cn*

[b] *Hebei Key Laboratory of Inorganic Nano-materials, College of Chemistry and Materials Science, Hebei Normal University, Shijiazhuang 050024, Hebei, China*

Covalent organic frameworks (COFs), as a class of crystalline porous polymers, are distinguished by their chemical tunability, persistent porosity, long-range ordering, and robust π–π conjugation networks.[13] These attributes make them promising platforms for designing and tailoring materials with precisely engineered reactive sites and electronic band structures, thus exhibiting great potential for diverse photocatalytic applications.[14] Their structural versatility enables exceptional performance in heavy metal reduction,[15,16] water splitting,[17–19] CO_2 conversion,[20–26] hydrogen peroxide (H_2O_2) production,[27–29] and organic transformations.[30–34] In particular, fine regulation of reactive oxygen species (ROS) generation efficiency through tailored COF linker modification at the molecular and atomic levels exhibits exceptional promise for selective photocatalytic oxidation processes.[35–37] Various functional units, including triazine,[38,39] benzothiadiazole,[40] and porphyrin moieties,[41] have been incorporated into COFs and demonstrated effective photooxidation performance under an oxygen atmosphere. To further optimize performance, donor–acceptor (D–A) configurations with specific energy levels are strategically engineered within COFs, which deliver concrete channels through precisely aligned π-conjugation for efficient charge separation and transfer.[42–45] Nonetheless, only a few COFs have achieved photocatalytic dipolar cycloaddition, and there has been a lack of in-depth studies on the O_2 reduction process until now. Additionally, due to the large exciton dissociation energy, achieving efficient photooxidation is still very difficult solely through D–A engineering. Therefore, it is highly desirable yet challenging to develop COF-based catalysts with high catalytic activity and excellent stability for photocatalytic dipolar [3 + 2] cycloaddition reactions.

Although D–A configurations have been demonstrated to enhance charge separation efficiency, the extent of electron delocalization within these structures remains constrained, limiting charge mobility.[46,47] To facilitate more efficient and rapid intramolecular charge transfer, it is crucial to establish an intrinsic driving force within the D–A system that promotes the delocalization of charge carriers around the photoexcitation sites. Fortunately, extending the π-conjugation system of COFs is an effective strategy to facilitate the separation and oriented transfer of photogenerated charge carriers[48–50] (Scheme 1c). However, while the conjugation degree or delocalized π-system has been seldom explored, how constitutional differences caused by conjugation effects can effectively regulate charge distribution remains largely unexplored. Accordingly, this study endeavors to delve into the influence of electronic delocalization in governing photocatalytic oxidation processes within D–A configured COFs, providing a new avenue for the formulation of more potent photocatalysts.

In this work, we strategically engineered the π-conjugated linkers of COFs (BD-COF, BT-COF, and BTDE-COF) to regulate charge distribution through molecular engineering concepts, aiming to enhance the efficiency of photocatalytic oxidative dipolar [3 + 2] cycloaddition reactions. By incorporating fully conjugated acetenyl π-spacers into D–A motifs, the charge separation and migration kinetics can be significantly optimized, resulting in a higher number of free charge carriers to drive the photocatalytic process. As a result, the BTDE-COF exhibits significantly enhanced photocatalytic activity for the tandem stepwise reaction of dipolar [3 + 2] cycloaddition (Scheme 1d), achieving superior yields of pyrrolo[2,1-*a*]isoquinolines compared to BD-COF and BT-COF. More importantly, the reaction also allows for gram-scale preparation in a mild and low-energy manner. Further experimental and theoretical results reveal that thiadiazole and acetenyl moieties contribute to the synergistic interplay between charge separation and oxygen adsorption to generate key ROS. The charge–oxygen synergy is crucial for initiating the cleavage of C–H bonds in pyrrolo[2,1-*a*]isoquinolines to achieve dipolar [3 + 2] cycloaddition with high performance. This work demonstrates a promising strategy to significantly boost photocatalytic oxidation by dual-engineered COF-based photocatalysts with charge–oxygen synergy.

Results and discussion

Three progressively upgraded COFs were synthesized *via* the condensation reaction in a solvothermal system. Specifically, [1,1′-biphenyl]-4,4′-dicarbaldehyde (BD-CHO), 4,4′-(benzo[*c*][1,2,5]thiadiazole-4,7-diyl)dibenzaldehyde (BT-CHO), 4,4′-(benzo[*c*][1,2,5]thiadiazole-4,7-diylbis(ethyne-2,1-diyl))dibenzaldehyde (BTDE-CHO) reacted with 4,4′,4″,4‴-(pyrene-1,3,6,8-tetrayl)tetraaniline (Py-NH_2) to produce BD-COF, BT-COF, and BTDE-COF, respectively (Fig. 1a). Elemental analysis (EA) revealed minor deviations between experimental and theoretical values (see experimental details in the SI), confirming the chemical purity and structural integrity of the synthesized COFs. The crystalline structures of these COFs were elucidated by powder X-ray diffraction (PXRD) measurements. In the PXRD patterns, BD-COF displays three prominent diffraction peaks at 3.2°, 6.4°, and 9.6° (Fig. 1b), corresponding to the (110), (220), and (330) facets, respectively. Compared to BD-COF, the (110) facet shifts toward lower degrees due to the extended pore size for BT-COF and BTDE-COF, in which prominent diffraction peaks at 2.7°, 5.5°, and 8.2° in BT-COF and 2.4°, 4.9°, and 7.3° in BTDE-COF can be observed (Fig. 1c and d), indicating their high crystallinity with similar rhombohedral lattices. The peaks centered at ∼23.5° are attributed to the (001) facets, which can be indexed to the π–π stacking. The experimental PXRD patterns of three COFs match well with their eclipsed AA-stacking models.

The chemical structures of the three COFs were then verified by a series of spectroscopic techniques. As evidenced by Fourier transform infrared (FT-IR) spectroscopy (Fig. 2a), the newly formed stretching vibration bands of the C═N bond are observed at ∼1624 cm^{-1}, indicating the successful construction of these COFs by imine linkages. Meanwhile, the disappearance of N–H (3300–3500 cm^{-1} for Py-NH_2) and C═O stretching vibration (∼1682 cm^{-1} for BD-CHO, BT-CHO, and BTDE-CHO) suggests the high polymerization of aldehyde and amine groups (Fig. S1–S3). In addition, BTDE-COF exhibits a characteristic C≡C stretching vibration at 2199 cm^{-1}, confirming the successful construction of acetenyl linkages. Solid-state ^{13}C cross-polarization magic angle spinning nuclear magnetic

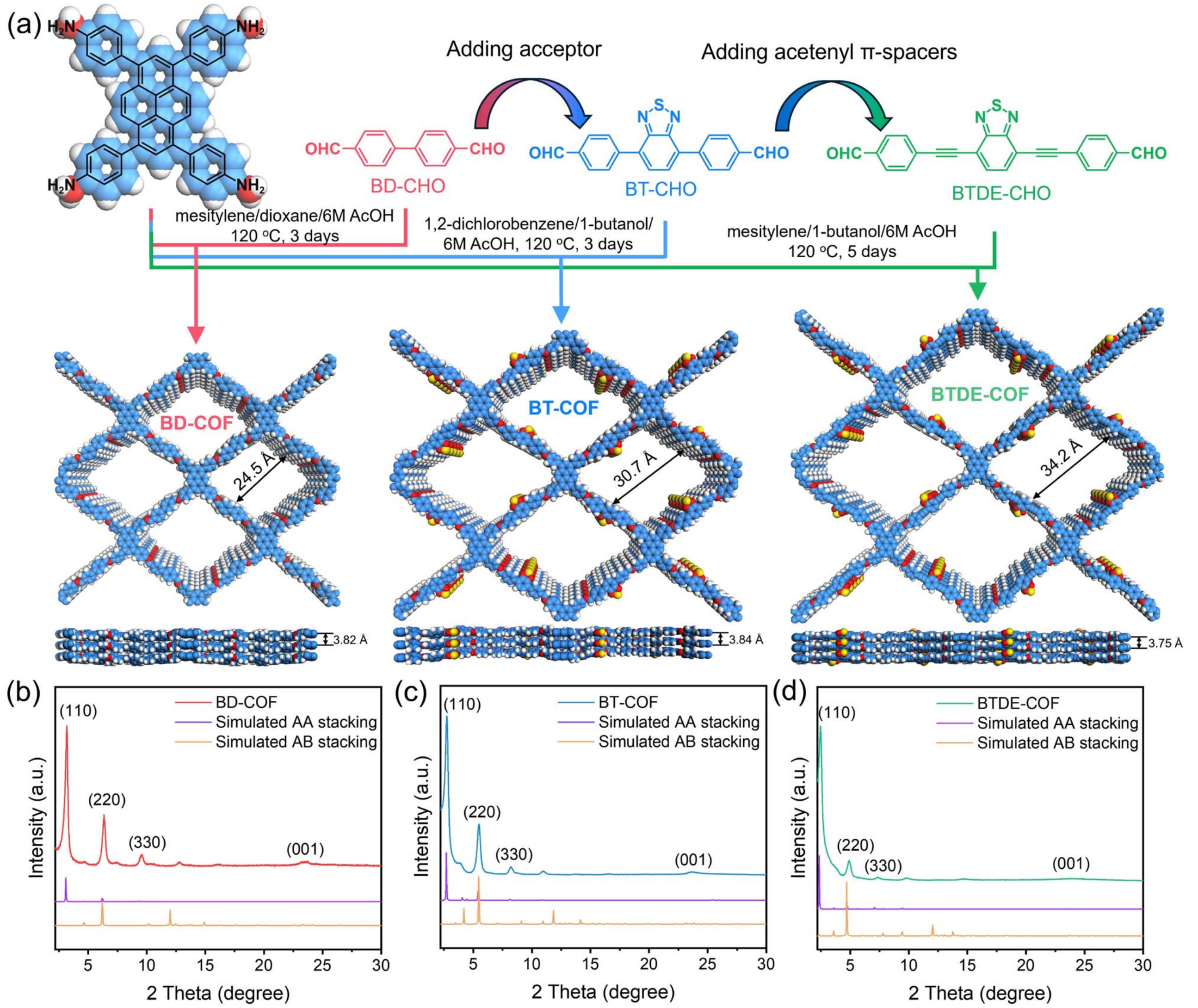

Fig. 1 (a) Schematic of the synthesis of BD-COF, BT-COF, and BTDE-COF. Simulated and experimental PXRD patterns of (b) BD-COF, (c) BT-COF, and (d) BTDE-COF.

resonance (CP/MAS NMR) (Fig. 2b) reveals distinct resonances at 156–160 ppm across all three COFs, corresponding to C=N carbon species, which substantiates the formation of Schiff-base networks. Notably, BT-COF and BTDE-COF display additional signals at ~154 ppm attributable to thiadiazole C–N bonds, while BTDE-COF specifically exhibits diagnostic peaks at 91 and 100 ppm characteristic of sp-hybridized acetenyl carbons. The aromatic carbon network is further corroborated by resonances spanning 120–140 ppm, consistent with pyrene-based building blocks. X-ray photoelectron spectroscopy (XPS) was also performed to further determine the chemical structures of the BTDE-COF, which specifically exhibits diagnostic peaks at 91 and 100 ppm characteristic of sp-hybridized acetenyl carbons. The aromatic carbon network is further corroborated by resonances spanning 120–140 ppm, consistent with pyrene-based building synthesized COFs. As shown in Fig. S4–S8, the high-resolution C 1s spectra for these COFs can be fitted into two peaks at ~284.8 and 285.6 eV, corresponding to the C=C/C–C and C=N/C–C bonds,[51] respectively. The high-resolution N 1s spectra of BD-COF show two signals at about 399.2 eV from the imine bonds and 400.0 eV from the residual N–H bonds; besides, the peaks belonging to C=N–S bonds can be fitted in the spectra of BT-COF and BTDE-COF. In particular, the S 2p XPS spectra of BT-COF and BTDE-COF reveal two peaks at about 162.0 and 163.2 eV, corresponding to S $2p_{3/2}$ and $2p_{1/2}$ from N=S=N groups,[52] respectively. This further confirms the successful formation of these COFs. Thermogravimetric analysis of all COFs shows a relatively high decomposition temperature of 500 °C, indicating excellent thermal stability (Fig. S9).

The permanent porosity characteristics of the synthesized COFs were quantitatively evaluated using nitrogen adsorption–desorption isotherms at 77 K. As depicted in Fig. 2c, all COFs exhibit typical type I isotherms with hysteresis loop structures, indicating their mesoporous feature. The Brunauer–Emmett–Teller (BET) surface areas of BD-COF, BT-COF, and BTDE-COF

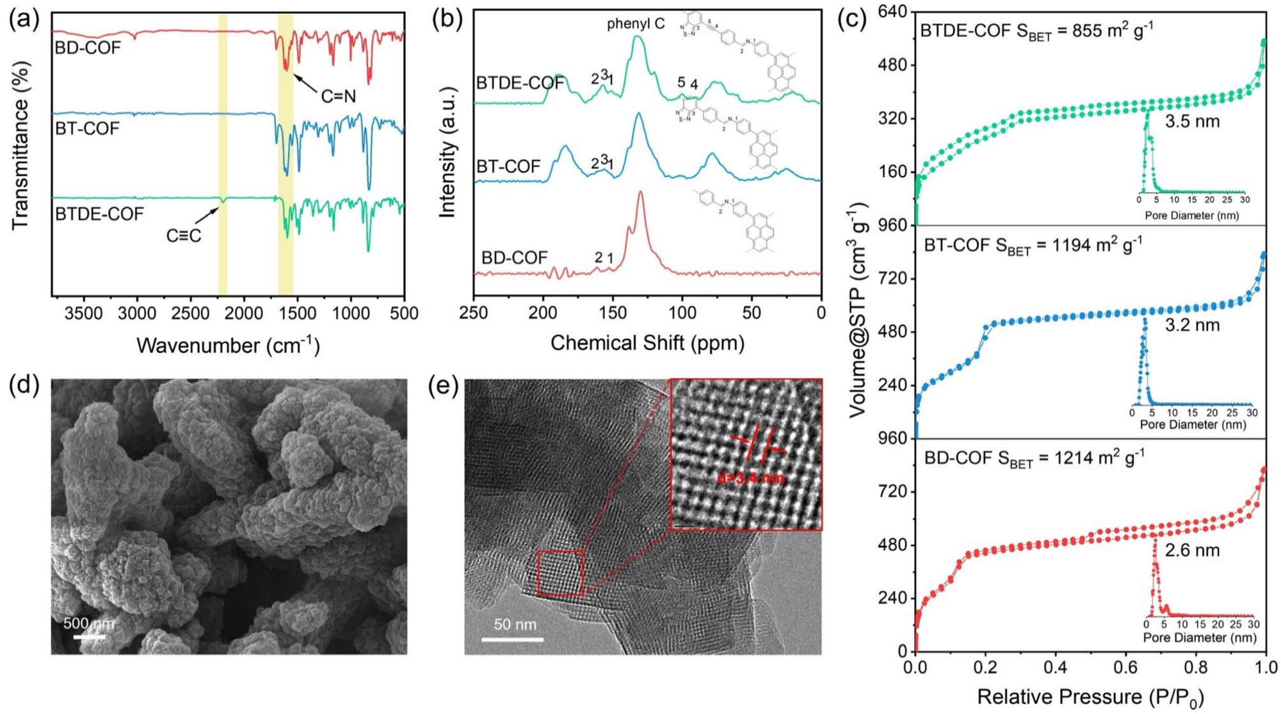

Fig. 2 (a) FT-IR spectra, (b) solid-state ^{13}C CP/MAS NMR spectra, and (c) nitrogen adsorption–desorption isotherms of BD-COF, BT-COF, and BTDE-COF. (d) SEM and (e) TEM images of BTDE-COF.

are calculated to be 1214, 1194, and 855 m^2 g^{-1}, respectively, indicative of significant surfaces that enhance photocatalytic interactions. Moreover, pore size distribution analysis using the non-local density functional theory (NLDFT) equilibrium model shows an average pore width of 2.6 nm for BD-COF, 3.2 nm for BT-COF, and 3.5 nm for BTDE-COF, consistent with the simulated AA stacking modes, providing additional evidence for the structural integrity and uniformity of the synthesized COFs. Scanning electron microscopy (SEM) and transmission electron microscopy (TEM) provided insights into the morphological features of these COFs, as shown in Fig. 2d, e, S10 and S11. Specifically, BD-COF exhibits flower-like morphology, while BT-COF and BTDE-COF display rod-like structures composed of smaller aggregated particles. The distinct one-dimensional channels with a uniform diameter of 2.4 nm for BD-COF, 3.0 nm for BT-COF, and 3.4 nm for BTDE-COF can be observed, which is consistent with the simulated structures.

The optical properties and band diagrams of the three COFs were investigated. Ultraviolet-visible diffuse reflectance spectroscopy (UV-vis DRS) in Fig. 3a shows broad absorption bands in the visible-light region. BT-COF and BTDE-COF exhibit an obvious redshift compared to BD-COF due to the incorporation of electron-withdrawing thiadiazole and conjugation-enhancing acetenyl units, which likely alter the conjugation pathways and energy levels within the COF framework. The optical bandgap (E_g) values of BD-COF, BT-COF, and BTDE-COF are ascertained to be 1.89, 1.75, and 1.60 eV, respectively, based on the Tauc plots. BTDE-COF with narrow E_g is more easily excited to generate photoinduced electrons and holes, enhancing its photocatalytic efficiency. Moreover, Mott–Schottky (M–S) curves (Fig. S12–S14) display the flat band positions of BD-COF, BT-COF, and BTDE-COF amounting to −0.93, −0.87, and −0.77 V (*vs.* Ag/AgCl), respectively. The positive slopes in the M–S plots indicate the n-type semiconductor properties of COFs; the conduction band potential (E_{CB}) is generally ∼0.2 V higher than the flat-band potential for n-type semiconductors.[53] Thus, the E_{CB} values for the COFs can be converted to −0.73, −0.67, and −0.57 V (*vs.* NHE). The energy band structures of the catalysts are depicted schematically in Fig. 3b. The E_{CB} potential of the three COFs has sufficient thermodynamic potential to drive O_2 reduction to the superoxide anion intermediate ($^{\bullet}O_2^-$, −0.33 V *vs.* NHE).[54] On the other hand, the valence band levels of BD-COF, BT-COF, and BTDE-COF are calculated to be +1.16, +1.08, and +1.03 V (*vs.* NHE), respectively, which are positive enough to allow the oxidation of ethyl 2-(3,4-dihydroisoquinolin-2(1*H*)-yl)acetate (**1a**) (0.73 V *vs.* NHE) through a photogenerated hole (Fig. S15).

Drawing on the above findings, the photocatalytic activities of COFs were assessed in the photocatalytic oxidative dipolar [3 + 2] cycloaddition of pyrrolo[2,1-*a*]isoquinoline under blue LED irradiation ($\lambda = 455$ nm) at room temperature. In a typical test, **1a** and *N*-phenylmaleimide (**2a**) were selected as model substrates, with oxygen acting as the environmentally benign oxidant, and dichloromethane (CH_2Cl_2) as the solvent. As expected, when employing BTDE-COF (5.0 mg) as the photocatalyst under an oxygen atmosphere for 1 h with the oxidant *N*-bromosuccinimide (NBS), product **3aa** was obtained in 74.4% yield (Fig. 3c and Table S1, entry 4). This result significantly

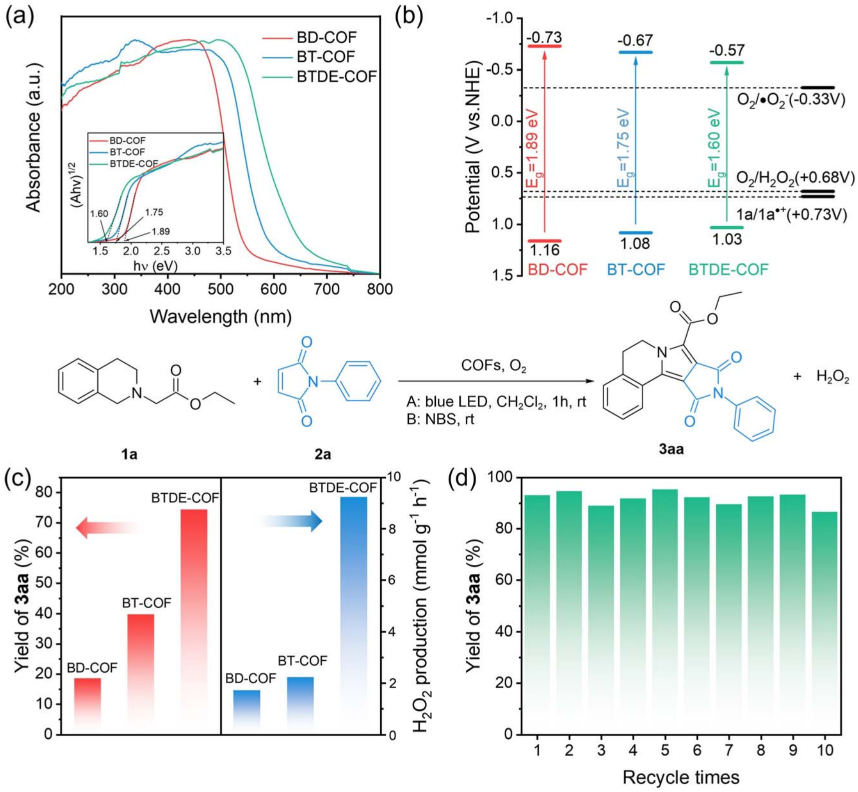

Fig. 3 (a) Solid-state UV-vis DRS spectra (inset: Tauc plots) and (b) electronic band structures of BD-COF, BT-COF, and BTDE-COF. (c) Photocatalytic performance for oxidative dipolar [3 + 2] cycloaddition over the three COF series. (d) Recycling stability of BTDE-COF for ten consecutive cycles of oxidative dipolar [3 + 2] cycloaddition for the synthesis of **3aa**.

surpassed the yields achieved with BD-COF (18.5%, Table S1, entry 2) and BT-COF (39.7%, Table S1, entry 3). This performance aligns with their respective photophysical properties, demonstrating the synergistic interaction between the thiadiazole and acetenyl units within BTDE-COF in driving the photocatalytic reaction. Apparent quantum efficiency (AQE) was calculated to be 0.60% for BD-COF, 1.29% for BT-COF, and 2.43% for BTDE-COF, respectively. Besides, H_2O_2 production was also detected, and thus, we measured the H_2O_2 production rate for the reaction mixtures using a UV spectrophotometer with the titanium ion detection method. The concentration of H_2O_2 produced was determined from the standard curve (Fig. S16). The H_2O_2 production rate could reach 9.24 mmol g^{-1} h^{-1} over BTDE-COF (Fig. 3c), significantly higher than that of BD-COF (1.71 mmol g^{-1} h^{-1}) and BT-COF (2.22 mmol g^{-1} h^{-1}), and this variation trend was consistent with the oxidation rate of **1a**. Screening of various solvents revealed that CH_2Cl_2 was the optimal solvent (Table S1, entries 5–9). Evaluation of catalyst equivalents demonstrated that reducing the equivalent amount resulted in a significant decrease in product yield (Table S1, entry 10), whereas increasing the photocatalyst loading showed minimal impact on the reaction outcome (Table S1, entry 11). To our delight, prolonging the reaction time could significantly boost the reaction yield to 93.1% (Table S1, entry 12), outperforming most of the previously reported catalytic systems (Table S2). Furthermore, controlled experiments demonstrated that the catalyst, light source, air, and NBS (Table S1, entries 13–16) all played a crucial role in the reactions. It was also discovered that white LEDs could drive the reaction as well, albeit with a decreased yield (45.3%, Table S1, entry 17).

The recyclability of BTDE-COF was subsequently assessed for photocatalytic oxidative [3 + 2] cycloaddition, using **1a** and **2a** as substrates under optimal conditions. The results indicated that BTDE-COF retained efficient catalytic performance after ten cycles (Fig. 3d). A hot filtration experiment by removing BTDE-COF after initiation of the cycloaddition reaction at 0.5 h revealed that the product yield had almost no change compared to that observed when the reaction was at 2 h (Fig. S17), demonstrating its typical heterogeneous catalyst nature. The sample of BTDE-COF after ten recycling tests was collected to analyze possible structural changes. FT-IR spectra (Fig. S18) showed that the chemical composition of BTDE-COF had negligible alterations. From the PXRD pattern of reused BTDE-COF after ten cycles (Fig. S19), although the intensity of the (110) diffraction peak weakened owing to extended exposure to the catalytic reaction and regeneration cycles, the diffraction peak remained distinct. This persistence confirms retention of the primary long-range order within the framework. Combined with the previously presented evidence, these findings demonstrate the high structural stability of BTDE-COF.

To explore the versatility of BTDE-COF, we tested the substituent effect of substrates, including *N*-substituted maleimides and tetrahydroisoquinolines. As shown in Scheme 2, the catalytic system was capable of oxidizing a diverse range of *N*-arylmaleimides substituted with both electron-withdrawing groups (**3ab–3af**, –F, –Cl, –Br, $–NO_2$, and –CN) and electron-donating groups (**3ag–3ai**, $–CH_3$, $–C_2H_5$, and $–OCH_3$) at the *para*-position of the aryl ring. The catalytic reaction consistently achieved high yields ranging from 87.1% to 94.2%, indicating that the electronic nature of the aryl ring had minimal influence on the catalytic activity. Moreover, *N*-benzylmaleimides (**3aj**, **3ak**) and *N*-alkylmaleimides (**3al–3ao**) also reacted smoothly under identical conditions, yielding the corresponding products in moderate-to-excellent yields. The scope of tetrahydroisoquinolines was examined by reacting with **2a**. Substituting the ethyl ester with a methyl ester (**3ba**) had no significant impact on the reaction efficiency, while a larger *tert*-butyl reduced the reactivity to afford the product by 61.3% (**3ca**). Additionally, replacing the carboxylic ester with a cyano group also led to a slightly lower yield (**3da**, 72.1%). These results highlighted the robustness of the catalytic system across different substituents, suggesting that it was well-suited for a broad spectrum of substrates. Most importantly, to further demonstrate the utility of this photocatalytic oxidative [3 + 2] cycloaddition over the BTDE-COF, we conducted a gram-scale reaction of **1a** (1.32 g) and **2a** (0.87 g) under standard conditions, smoothly affording product **3aa** in 87.5% yield (1.69 g). In summary, BTDE-COF exhibited outstanding catalytic performance, exceptional stability, and notable universality, rendering it a promising candidate for the synthesis of pyrrolo[2,1-*a*]isoquinolines *via* photocatalytic oxidative [3 + 2] cycloaddition.

To reveal insights into the enhancement of the photocatalytic performance of BTDE-COF, the charge transfer and separation behavior of COFs were fully characterized with various techniques. Transient photocurrent responses (Fig. 4a)

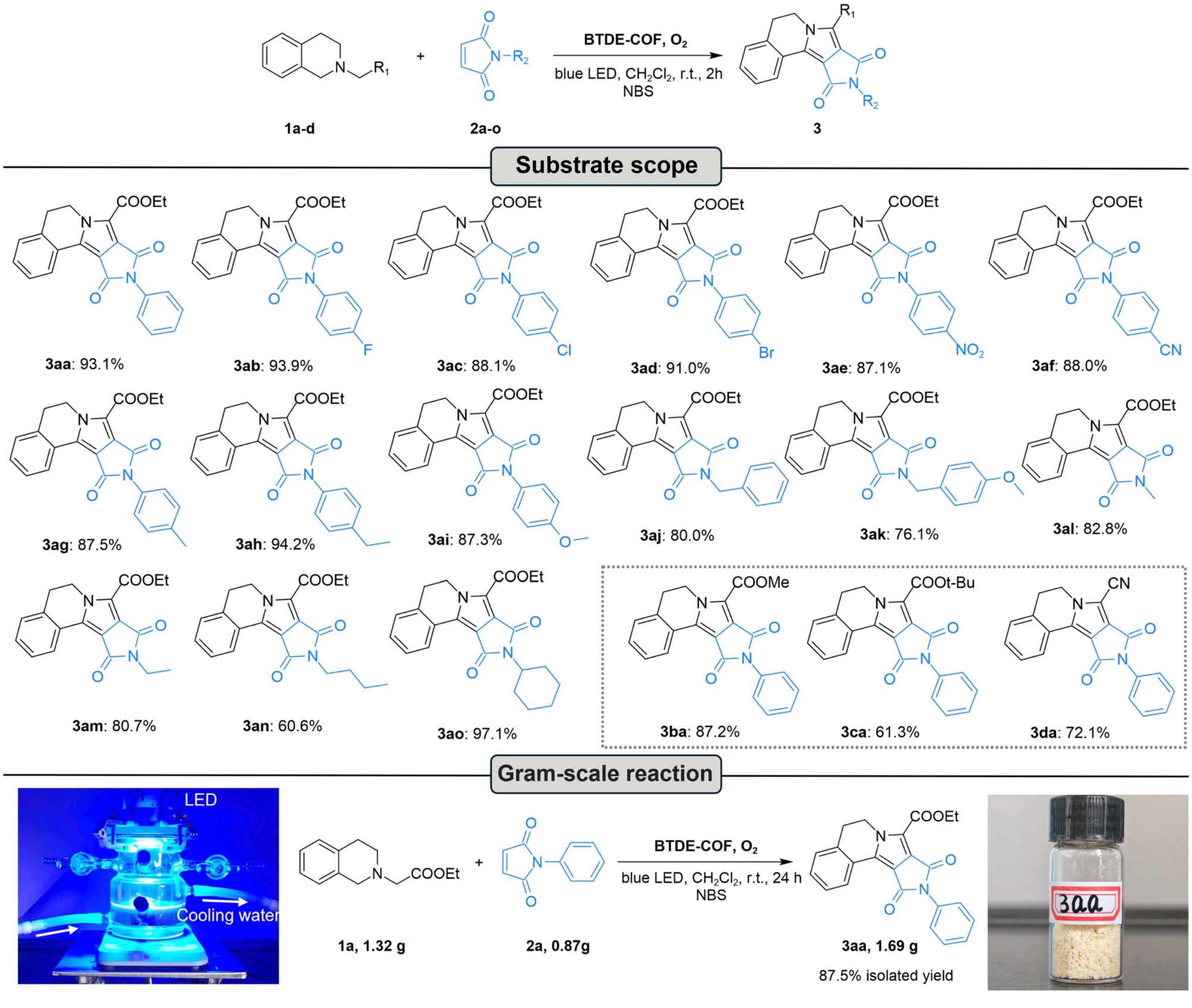

Scheme 2 Substrate scope and gram-scale reaction for photocatalytic oxidative dipolar [3 + 2] cycloaddition over BTDE-COF. Reaction conditions: step (A): **1a–d** (0.12 mmol), **2a–o** (0.1 mmol), BTDE-COF (5 mg), CH_2Cl_2 (4 mL), bubbled with O_2 for 10 min, and blue LEDs ($\lambda = 455$ nm) for 2 h at room temperature. Step (B): NBS (1.1 equiv.) was added to the reaction mixture and stirred for another 1 h.

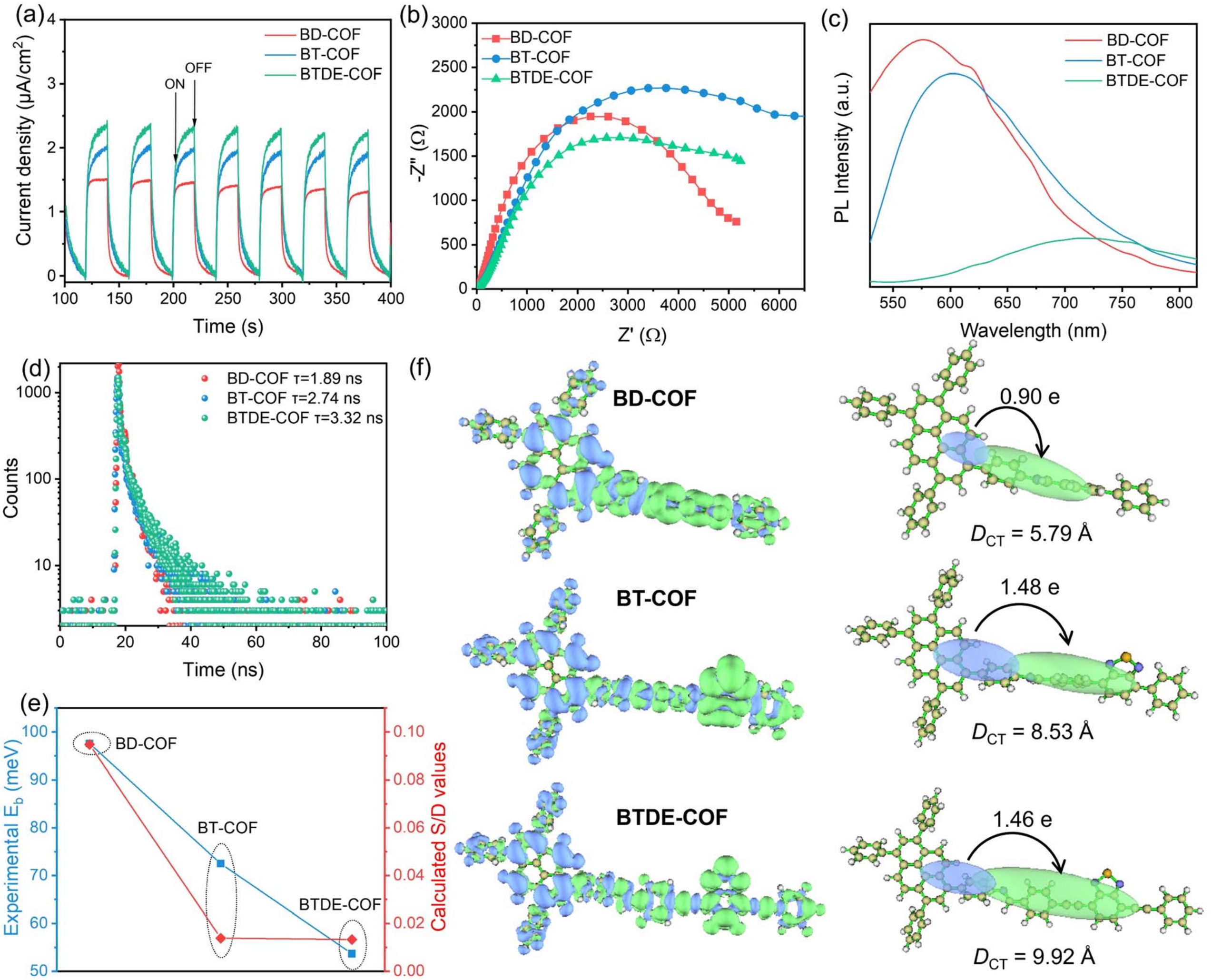

Fig. 4 (a) Transient photocurrent responses, (b) EIS curves, (c) PL spectra, (d) TR-PL plots, and (e) experimental E_b value and calculated S/D value (S represents the calculated overlap of hole–electron distribution and D represents the calculated distance between holes and electrons) of BD-COF, BT-COF, and BTDE-COF. (f) Computed charge density difference between the ground and the excited states at an isovalue of 0.0005 a.u. ($\Delta\rho$ is shown above and centroids of charges are shown below). Green and blue represent an increase and decrease in electron density, respectively. Quantitative charge-transfer analysis is based on the atomic dipole corrected Hirshfeld (ADCH) atomic charges. D_{CT} represents the distance between the barycenter of the density increment and depletion regions upon electronic excitation.

and electrochemical impedance spectroscopy (EIS) Nyquist plots (Fig. 4b) were obtained to investigate the charge separation and transport of the COF series. BTDE-COF exhibits a larger transient photocurrent density and a smaller radius of the Nyquist semicircle, suggesting a higher charge separation efficiency than BD-COF and BT-COF. Photogenerated carrier recombination in the COFs was also characterized by photoluminescence (PL) and time-resolved photoluminescence (TR-PL) measurements. As shown in Fig. 4c, the PL intensities of the COFs are in the order BTDE-COF < BT-COF < BD-COF, implying a strong suppression of radiative exciton recombination in BTDE-COF. Moreover, the PL emission peaks of BTDE-COF and BT-COF exhibit a progressive redshift compared to BD-COF, consistent with the change in their bandgaps. TR-PL measurements reveal the corresponding lifetimes with the same variation trend of emission intensities (Fig. 4d). The calculated fluorescence lifetime of BTDE-COF is found to increase to 3.32 ns, in contrast to BD-COF (1.89 ns) and BT-COF (2.74 ns), implying that the photogenerated electrons formed by BTDE-COF can persist in the excited state for a relatively long time. Temperature-dependent photoluminescence (TD-PL) spectroscopy was further performed to gain insights into their charge-separation behavior (Fig. 4e, blue line, and Fig. S20–S22). The integrated PL intensities of the three COFs increase with decreasing temperature, which is associated with the thermally activated non-radiative recombination process. The exciton binding energy is fitted with the Arrhenius equation: $I(T) = I_0/(1 + A\exp(-E_b/k_BT))$, where I_0 is the intensity at 0 K, k_B is the Boltzmann constant, and E_b is the exciton binding energy.[55] The exciton binding energies (E_b) can be fitted to 97.6 meV for BD-COF, 72.5 meV for BT-COF, and 53.7 meV for BTDE-COF, respectively. The lower E_b value of BTDE-COF indicates enhanced dissociation capability compared to BD-COF and BT-COF. These spectral characteristics suggest that the synergistic combination of thiadiazole and acetenyl units can effectively minimize the E_b and facilitate efficient charge separation and migration processes, in favor of generating more free charge carriers to drive the photocatalytic process. Furthermore, the direction of electronic transport of COF_{DFT} was investigated through density functional theory (DFT) calculations using Gaussian 09 software. The highest occupied molecular orbitals (HOMOs) of COF_{DFT} are found to be concentrated on pyrene moieties (the donor component), while their lowest unoccupied molecular orbitals (LUMOs) are localized on phenyl and thiadiazole moieties (the acceptor component), illustrating a typical donor–acceptor (D–A) heterostructure (Fig. S23). Such a structure effectively inhibits the recombination of photogenerated electrons and holes. Notably, compared to BD-COF_{DFT}, both BT-COF_{DFT} and BTDE-COF_{DFT} containing electron-withdrawing thiadiazole moieties demonstrate a more distinct spatial separation between the LUMO and HOMO. The theoretically calculated bandgap (E_g) of BTDE-COF_{DFT} is lower than that of BD-COF_{DFT} and BT-COF_{DFT}, which is consistent with the above experimental results. The electrostatic potential (ESP) distributions of the three model structures show that the potential difference between BT-COF_{DFT} and BTDE-COF_{DFT} is more pronounced compared to the weak electrostatic interaction of BD-COF_{DFT}. Additionally, BTDE-COF_{DFT} exhibits a significantly higher molecular dipole moment (2.81 D) compared to BD-COF_{DFT} (1.78 D) and BT-COF_{DFT} (2.73 D). This enhanced dipole indicates a stronger internal electric field within BTDE-COF_{DFT}, facilitating the separation of photo-generated charge carriers and improving photocatalytic efficiency.[56,57]

Time-dependent density functional theory (TD-DFT) calculations were conducted to ascertain the distribution of electrons and holes in the excited state. Based on the hole–electron analysis using *Multiwfn* software,[58,59] the hole and electron can be differentiated by S/D values,[60] where S denotes the computed overlap integral between hole and electron distributions, while D represents the calculated centroid-to-centroid separation distance between the hole and electron densities. Therefore, a smaller S paired with a larger D corresponds to more pronounced charge transfer characteristics.[61] The computed S/D values of BT-COF_{DFT} and BTDE-COF_{DFT} are significantly lower than that of BD-COF_{DFT} (Fig. 4e, red line, Table S3) and correspond to lower exciton binding energy (Fig. S24); nevertheless, these parameters of BTDE-COF_{DFT} are very close to those of BT-COF_{DFT}. These results indicate that the thiadiazole unit is favorable for charge transfer. Additionally, the intramolecular charge transfer effect was confirmed by analyzing the contributions of nonhydrogen atoms to holes and electrons in the excited state (Fig. S25 and S26). In BT-COF_{DFT}, holes were mainly concentrated in pyrene segments and electrons in the thiadiazole segments, whereas in BTDE-COF_{DFT}, alkynyl segments also have a small number of electrons.

The charge density difference between the ground and the excited states is adopted to visualize the electron transfer within COFs.[62,63] Spatial separation of charge centroids reveals distinct localization of positive and negative charges in their two respective segments, while the overlapping regions suggest a hybrid local and charge-transfer excited state in these COFs (Fig. 4f). Quantitative evaluation of charge separation efficiency was performed by calculating two critical parameters: electron–hole distribution centroid distance (D_{CT}) and transferred electron amount during photoexcitation. The larger D_{CT} value and the higher transferred electron amount denote a stronger charge transfer process. Notably, BTDE-COF_{DFT} features the largest D_{CT} value (9.92 Å) accompanied by an electron transfer amount (1.46e). This trend parallels the observed S/D value variations, establishing a direct correlation between enhanced D–A interaction strength and improved charge transfer dynamics. The exceptional charge separation metrics of BTDE-COF rationalize its optimal photocatalytic performance, as strengthened D–A interactions effectively suppress carrier recombination while facilitating directional charge migration.

To clarify the mechanism of photocatalytic oxidative [3 + 2] cycloaddition, we initially performed a series of quenching experiments. As shown in Fig. 5a, the desired reaction is significantly inhibited by $CuSO_4$ (as an electron scavenger) and KI (as the hole scavenger), suggesting that the redox process is primarily triggered by the photoinduced electron–hole pair generated on BTDE-COF. To identify the reactive species involved, we employed hydroquinone (HQ), *p*-benzoquinone (*p*-BQ), 2,2,6,6-tetramethyl-1-piperidinyloxy (TEMPO), and *tert*-butyl alcohol (*t*-BuOH) as scavengers for free radicals, superoxide radicals ($^{\bullet}O_2^-$), singlet oxygen ($^1O_2$), and hydroxyl radicals ($^{\bullet}OH$), respectively. The experimental results reveal that the reaction predominantly involves the free radical and $^{\bullet}O_2^-$ species. Electron spin resonance (ESR) analysis was conducted to further verify the ROS produced by BTDE-COF during photocatalysis. The ESR results demonstrate that BTDE-COF significantly enhances $^{\bullet}O_2^-$ signals under illumination when using DMPO (5,5-dimethyl-1-pyrroline-*N*-oxide) as a spin-trapping agent (Fig. 5b). In contrast, only weak $^1O_2$ signals were observed using TEMP (2,2,6,6-tetramethyl-4-piperidone) as a spin-trapping agent (Fig. S27), which is consistent with the results from the quenching experiments and revealed the dominant role of $^{\bullet}O_2^-$ in the reaction.

Subsequently, we conducted a detailed investigation into the active sites on BTDE-COF using *in situ* diffuse reflectance infrared Fourier transform spectroscopy (DRIFTS). Initially, an O_2 atmosphere was used to identify the active sites for the oxygen reduction reaction (ORR). After exposure to O_2 under irradiation, the peaks observed at 869, 1024, and 1173 cm^{-1} are assigned to O–O, C–O–O, and $^{\bullet}O_2^-$ (Fig. 5c),[54,64] respectively, indicating the occurrence of the ORR, and the peak intensity is significantly increased with the irradiation. Meanwhile, the significant changes in the intensity of acetenyl peaks (2176 cm^{-1}) indicated that the adsorbed O_2 at these sites participates in the ORR (Fig. 5d).[65] The peaks belonging to C=N–S also show obvious variations, accompanied by the emergence of a notable peak around 1750 cm^{-1}, ascribed to the N–O bond formed with the pyridine nitrogen of thiadiazole during O_2 reduction.[66] Moreover, we further conducted an *in situ* test under O_2 and **1a** conditions to explore the reaction process on the surface of BTDE-COF (Fig. 5e). Under irradiation, the

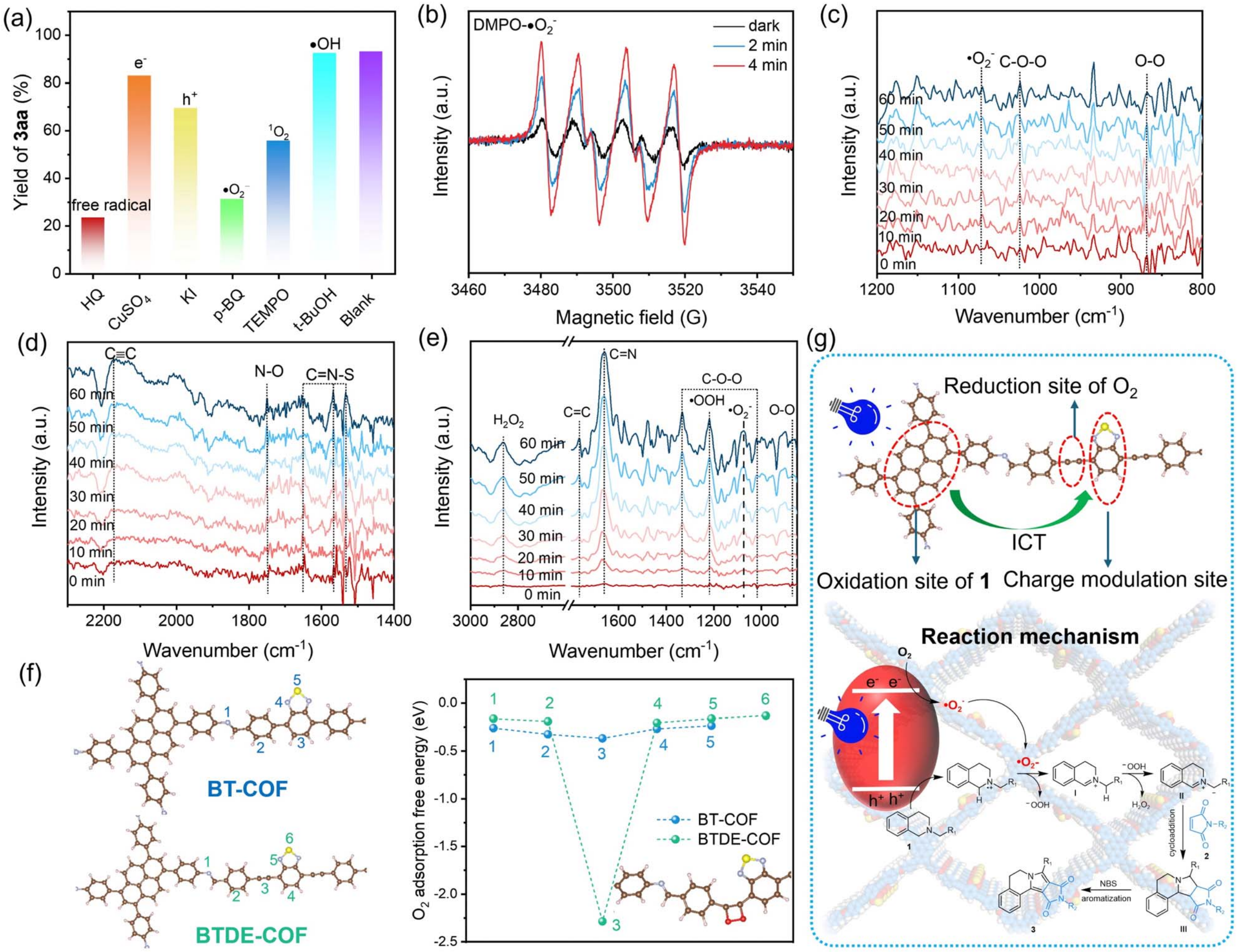

Fig. 5 (a) Yield of **3aa** over BTDE-COF in the presence of scavengers for reactive oxygen species under illumination for 2 h in O_2. (b) ESR spectra of DMPO–$^{\bullet}O_2^-$ for BTDE-COF under illumination. *In situ* DRIFTS spectra of BTDE-COF under irradiation: (c and d) in an O_2 atmosphere and (e) under O_2 + **1a** conditions. (f) The adsorption energy of O_2 on the optimum site of BTDE-COF. (g) The proposed mechanism for photocatalytic oxidative [3 + 2] cycloaddition over BTDE-COF.

emergence of *OOH (1289 cm^{-1})[67] is observed during the photocatalytic process when adding **1a** into the system. This corresponds to the protonation of $^{\bullet}O_2^-$ ($*^{\bullet}O_2^- + H^+ \rightarrow *OOH$), which occurred as a result of the oxidation of **1a**. The peak at 2860 cm^{-1} is attributed to the O–H bending vibration of H_2O_2. Additionally, the characteristic peaks of the C═N bond (1679 cm^{-1}) are also observed in DRIFTS,[68] attributed to the produced intermediate products of **1a** during photocatalysis. As the irradiation time increases, the vibrations of these bands gradually intensify, further substantiating the hypothesis of photocatalytic oxidative [3 + 2] cycloaddition coupled with O_2 reduction.

Furthermore, DFT calculations were conducted to further determine active sites on BTDE-COF. Based on the HOMO and LUMO of BTDE-COF, the active sites are centered at benzo[*c*][1,2,5]thiadiazole and the adjacent alkynyl segment, while pyrene units are identified as predominant oxidation sites (Fig. 5f). Accordingly, DFT calculations were then performed to unveil the plausible oxygen adsorption sites within BT-COF and BTDE-COF (Fig. 5f). Calculations of O_2 adsorption energy in BT-COF reveal that the adsorption energy of phenyl carbon atoms of benzo[*c*][1,2,5]thiadiazole in BT-COF ($E_{abs} = -0.37$ eV) is lower than that of other sites. However, the adsorption energy for O_2 on acetenyl sites (site-3) of BTDE-COF ($E_{abs} = -2.28$ eV) is notably lower than that of phenyl carbon atoms of benzo[*c*][1,2,5]thiadiazole (site-4). This suggests preferential O_2 chemisorption at the electron-rich acetenyl sites, facilitating subsequent formation of metastable endoperoxide intermediates (*OO*) through electron transfer processes. These findings reveal that the acetenyl units serve as primary oxygen reduction centers for superoxide radical ($^{\bullet}O_2^-$) generation, while the thiadiazole components promote the intramolecular charge transfer (ICT) and facilitate their rapid transfer to O_2 through their electron-deficient character. This charge–oxygen synergy boosts the overall efficiency of the photocatalytic dipolar [3 + 2] cycloaddition reaction *via* simultaneous substrate activation and reactive oxygen species generation.

Based on the above discussions and previous reports,[69–71] the proposed mechanism for photocatalytic oxidative [3 + 2] cycloaddition is illustrated in Fig. 5g. Under visible-light irradiation, BTDE-COF is excited to a higher energy state and undergoes charge separation, generating electrons (e^-) and holes (h^+). The electrons reduce molecular oxygen to form $^{\bullet}O_2^-$, while the holes oxidize **1** to its radical cation intermediate ($\mathbf{1}^{\bullet+}$). This $^{\bullet}O_2^-$ subsequently abstracts one proton from intermediate $\mathbf{1}^{\bullet+}$, leading to the formation of intermediate **I** and $^{\bullet}OOH$. The generated $^{\bullet}OOH$ then captures an electron and another proton from **I**, forming 1,3-dipole azomethine **II** and releasing a H_2O_2 molecule. Following this, intermediate **II** undergoes a [3 + 2] cycloaddition with dipolarophile **2**, yielding hexahydropyrrolo [2,1-*a*]isoquinoline **III**. Finally, the oxidative aromatization of **III** in the presence of the oxidant NBS leads to the formation of the target product **3**.

Conclusions

In summary, we proposed a charge–oxygen synergy strategy through dual-engineered COFs by integrating π-spacers with donor–acceptor motifs to promote intermolecular cycloaddition. Experimental investigations and DFT calculations demonstrated that the incorporation of electron-withdrawing thiadiazole units enhances the charge separation efficiency of the photocatalysts, and the strongly conjugated acetenyl units promoted spontaneous oxygen adsorption to stabilize endoperoxide intermediate species, leading to more efficient ROS generation to subsequently initiate the cleavage of C–H bonds in pyrrolo[2,1-*a*]isoquinolines. As a result, the optimized BTDE-COF exhibits significantly enhanced activity for the photocatalytic oxidative dipolar [3 + 2] cycloaddition reaction under mild conditions, producing pyrrolo[2,1-*a*]isoquinolines in high yields. It was superior to the corresponding BD-COF and BT-COF. This work offers insight into regulating multistep charge transport and designing efficient metal-free COF-based photocatalysts.

Author contributions

Y. L. carried out the synthesis of materials and photocatalytic experiments. L. S., H. Y. and X. Z. characterized these materials. X. L. conducted DFT calculations, wrote the manuscript, and supervised the project. All authors discussed the results and contributed to the preparation of the manuscript.

Conflicts of interest

There are no conflicts to declare.

Data availability

The data supporting this article have been included as part of the SI. Supplementary information: experimental details on the synthesis of materials, supplementary characterizations, segmental catalytic data, and NMR data. See DOI: **https://doi.org/10.1039/d5sc04639d**.

Acknowledgements

This work was financially supported by the National Natural Science Foundation of China (21908038), Natural Science Foundation of Hebei Province (B2024201017 and B2023201108), Science Research Project of Hebei Education Department (BJK2022001), Hebei Province Innovation Capability Enhancement Plan Project (22567632H), and Youth Top Talent Project of Hebei University. The authors also acknowledge the High-Performance Computing Center of Hebei University.

Notes and references

1 X.-M. Xu, L. Zhao, J. Zhu and M.-X. Wang, *Angew. Chem., Int. Ed.*, 2016, **55**, 3799–3803.
2 H.-L. Cui, *Org. Biomol. Chem.*, 2022, **20**, 2779–2801.
3 W. Xi, Y. Zhang, H. Wu, J. Li, Y. Wang, J. Yang, Z. Wang and W. Yao, *Org. Lett.*, 2023, **25**, 4908–4912.
4 N. M. Moreira, I. T. Miranda, J. R. N. D. Santos, T. Opatz, G. Oliva, R. V. C. Guido and A. G. Corrêa, *J. Org. Chem.*, 2023, **88**, 8781–8790.
5 Q. Tang, Y. Liu, B. Fei, Q. Tao, C. Wang, X. Jiang, X. He and Y. Shang, *J. Org. Chem.*, 2024, **89**, 8420–8434.
6 K. Zheng, S. Zhuang, W. Shu, Y. Wu, C. Yang and A. Wu, *Chem. Commun.*, 2018, **54**, 11897–11900.
7 Y.-Q. Zou, L.-Q. Lu, L. Fu, N.-J. Chang, J. Rong, J.-R. Chen and W.-J. Xiao, *Angew. Chem., Int. Ed.*, 2011, **50**, 7171–7175.
8 M. Escolano, D. Gaviña, G. Alzuet-Piña, S. Díaz-Oltra, M. Sánchez-Roselló and C. Pozo, *Chem. Rev.*, 2024, **124**, 1122–1246.
9 T. P. Yoon, M. A. Ischay and J. Du, *Nat. Chem.*, 2010, **2**, 527–532.
10 Y. Wen, H.-X. Jin, Y.-H. Qiu, Y. Zong, W. Luo, Z. Chen and D. Yu, *Chem. Commun.*, 2024, **60**, 4573–4576.
11 Z.-Q. Yi, W. Zhang, B. Yi, C. Liu, Y. Xie, M. Li, Y. Xiong, W. Wu and J.-P. Tan, *Org. Lett.*, 2025, **27**, 2197–2202.
12 A. Fujiya, M. Tanaka, E. Yamaguchi, N. Tada and A. Itoh, *J. Org. Chem.*, 2016, **81**, 7262–7270.
13 K.-T. Tan, S. Ghosh, Z. Wang, F. Wen, D. Rodríguez-San-Miguel, J. Feng, N. Huang, W. Wang, F. Zamora, X. Feng, A. Thomas and D. Jiang, *Nat. Rev. Methods Primers*, 2023, **3**, 1.
14 Y. Chen and D. Jiang, *Acc. Chem. Res.*, 2024, **57**, 3182–3193.
15 X. Ma, K. R. Meihaus, Y. Yang, Y. Zheng, F. Cui, J. Li, Y. Zhao, B. Jiang, Y. Yuan, J.-R. Long and G. Zhu, *J. Am. Chem. Soc.*, 2024, **146**, 23566–23573.
16 H. Yang, M. Hao, Y. Xie, X. Liu, Y. Liu, Z. Chen, X. Wang, G. I. N. Waterhouse and S. Ma, *Angew. Chem., Int. Ed.*, 2023, **62**, e202303129.
17 J. Cheng, Y. Wu, W. Zhang, J. Zhang, L. Wang, M. Zhou, F. Fan, X. Wu and H. Xu, *Adv. Mater.*, 2024, **36**, 2305313.
18 Y. Yang, X. Chu, H.-Y. Zhang, R. Zhang, Y.-H. Liu, F.-M. Zhang, M. Lu, Z.-D. Yang and Y.-Q. Lan, *Nat. Commun.*, 2023, **14**, 593.
19 L. Zou, D. Si, S. Yang, Z. Chen, Y. Huang and R. Cao, *Angew. Chem., Int. Ed.*, 2025, **64**, e202418319.

20 X. Lan, H. Li, Y. Liu, Y. Zhang, T. Zhang and Y. Chen, *Angew. Chem., Int. Ed.*, 2024, **136**, e202407092.

21 P. Fu, C. Chen, C. Wu, B. Meng, Q. Yue, T. Chen, W. Yin, X. Chi, X. Yu, R. Li, Y. Wang, Y. Zhang, W. Luo, X. Liu, Y. Han, J. Wang, S. Xi and Y. Zhou, *Angew. Chem., Int. Ed.*, 2025, **64**, e202415202.

22 S. Gao, Q. Zhang, X. Su, X. Wu, X.-G. Zhang, Y. Guo, Z. Li, J. Wei, H. Wang and S. Zhang, *J. Am. Chem. Soc.*, 2023, **145**, 9520–9529.

23 Q. Xu, J. Han, F. Tian, X. Zhao, J. Rong, J. Zhang, P. She, J.-S. Qin and H. Rao, *J. Am. Chem. Soc.*, 2025, **147**, 10587–10597.

24 Y. Yang, H.-Y. Zhang, Y. Wang, L.-H. Shao, L. Fang, H. Dong, M. Lu, L.-Z. Dong, Y.-Q. Lan and F.-M. Zhang, *Adv. Mater.*, 2023, **35**, 2304170.

25 Y. Huang, P. Du, W.-X. Shi, Y. Wang, S. Yao, Z.-M. Zhang, T.-B. Lu and X. Lu, *Appl. Catal., B*, 2021, **288**, 120001.

26 H.-Q. Yin, Z.-M. Zhang and T.-B. Lu, *Acc. Chem. Res.*, 2023, **56**, 2676–2687.

27 J.-Y. Yue, L.-P. Song, Y.-F. Fan, Z.-X. Pan, P. Yang, Y. Ma, Q. Xu and B. Tang, *Angew. Chem., Int. Ed.*, 2023, **62**, e202309624.

28 T. Yang, D. Zhang, A. Kong, Y. Zou, L. Yuan, C. Liu, S. Luo, G. Wei and C. Yu, *Angew. Chem., Int. Ed.*, 2024, **63**, e202404077.

29 F. Zhang, X. Lv, H. Wang, J. Cai, H. Wang, S. Bi, R. Wei, C. Yang, G. Zheng and Q. Han, *Adv. Mater.*, 2025, **37**, 2502220.

30 A. Alam, M. Roy, S. Maji, A. Chakraborty, V. Singh, A. Kumar, S. Mondal, A. Banerjee, K. Kailasam, D. Adhikari and P. Pachfule, *Adv. Mater.*, 2025, **37**, 2416100.

31 H. Chen, H.-S. Jena, X. Feng, K. Leus and P. Van Der Voort, *Angew. Chem., Int. Ed.*, 2022, **61**, e202204938.

32 M. Traxler, S. Gisbertz, P. Pachfule, J. Schmidt, J. Roeser, S. Reischauer, J. Rabeah, B. Pieber and A. Thomas, *Angew. Chem., Int. Ed.*, 2022, **61**, e202117738.

33 H. Hao, F. Zhang, X. Wang, F. Huang, S. Chen and X. Lang, *Adv. Funct. Mater.*, 2025, **35**, 2419735.

34 P. Huang, M.-Y. Yang, S.-B. Zhang, Z.-H. Li, H. Zhang, S.-M. Wang, Y.-Y. Peng, M. Zhang, S.-L. Li, M. Lu and Y.-Q. Lan, *Angew. Chem., Int. Ed.*, 2025, **64**, e202423091.

35 S. Suleman, Y. Zhang, Y. Qian, J. Zhang, Z. Lin, Ö. Metin, Z. Meng and H.-L. Jiang, *Angew. Chem., Int. Ed.*, 2024, **63**, e202314988.

36 Q. Xue, H. Li, P. Jin, X. Zhou and F. Wang, *Angew. Chem., Int. Ed.*, 2025, **64**, e202423368.

37 T. Yang, F. Kong, Y. Chen, A. Kong, X. Cui and J. Shi, *Angew. Chem., Int. Ed.*, 2025, **64**, e202424110.

38 S. Li, N. Huber, W. Huang, W. Wei, K. Landfester, C.-T. Ferguson, Y. Zhao and K.-A. Zhang, *Angew. Chem., Int. Ed.*, 2024, **63**, e202400101.

39 J. Tang, Z. Jiang, Z. Gao, Q. Xie, S. Gu, A. Chen, J. Yuan, W. Li, R. Tang and G. Yu, *Angew. Chem., Int. Ed.*, 2025, **64**, e202416879.

40 R. Liu, Y. Chen, H. Yu, M. Položij, Y. Guo, T.-C. Sum, T. Heine and D. Jiang, *Nat. Catal.*, 2024, **7**, 195–206.

41 J.-L. Shi, R. Chen, H. Hao, C. Wang and X. Lang, *Angew. Chem., Int. Ed.*, 2020, **59**, 9088–9093.

42 X. Wang, H. Li, S. Zhou, J. Ning, H. Wei, X. Li, S. Wang, L. Hao and D. Cao, *Adv. Funct. Mater.*, 2025, **35**, 2424035.

43 J. Liu, C. Tuo, W.-Y. Xiao, M.-Y. Qi, Y. Yusran, Z. Wang, H. Li, C. Guo, J. Song and S. Qiu, *Angew. Chem., Int. Ed.*, 2025, **64**, e202416240.

44 Z.-A. Lan, G. Zhang, X. Chen, Y. Zhang, K.-A. Zhang and X. Wang, *Angew. Chem., Int. Ed.*, 2019, **58**, 10236–10240.

45 Y.-Z. Peng, G.-C. Guo, S. Guo, L.-H. Kong, T.-B. Lu and Z.-M. Zhang, *Angew. Chem., Int. Ed.*, 2021, **60**, 22062–22069.

46 Y. Xia, W. Zhang, S. Yang, L. Wang and G. Yu, *Adv. Mater.*, 2023, **35**, 2301190.

47 L. Wang and W. Zhu, *Adv. Sci.*, 2024, **11**, 2307227.

48 X.-X. Wang, C.-R. Zhang, R.-X. Bi, Z.-H. Peng, A.-M. Song, R. Zhang, H.-X. He, J.-X. Qi, J.-W. Gong, C.-P. Niu, R.-P. Liang and J.-D. Qiu, *Adv. Funct. Mater.*, 2025, **35**, 2421623.

49 Z. Li, T. Deng, S. Ma, Z. Zhang, G. Wu, J. Wang, Q. Li, H. Xia, S. W. Yang and X. Liu, *J. Am. Chem. Soc.*, 2023, **145**, 8364–8374.

50 F. Meng, J. Wang, M. Chen, Z. Wang, G. Bai and X. Lan, *ACS Catal.*, 2023, **13**, 12142–12152.

51 Z. Zhao, Y. Zheng, C. Wang, S. Zhang, J. Song, Y. Li, S. Ma, P. Cheng, Z. Zhang and Y. Chen, *ACS Catal.*, 2021, **11**, 2098–2107.

52 F. Zhang, Y. Wang, Q. Zhao, H. Zhao, X. Dong, X.-K. Gu, H. Sheng, S. Sarina and X. Lang, *ACS Appl. Mater. Interfaces*, 2024, **17**, 1097–1109.

53 Y. Zhang, Y. Liu, H. Li, G. Bai and X. Lan, *Chem. Eng. J.*, 2024, **489**, 151479.

54 W. Wu, Z. Li, S. Liu, D. Zhang, B. Cai, Y. Liang, M. Wu, Y. Liao and X. Zhao, *Angew. Chem., Int. Ed.*, 2024, **63**, e202404563.

55 J. Xu, C. Yang, S. Bi, W. Wang, Y. He, D. Wu, Q. Liang, X. Wang and F. Zhang, *Angew. Chem., Int. Ed.*, 2020, **59**, 24053–24061.

56 M. Liu, C. X. Cui, S. Yang, X. Yang, X. Li, J. He, Q. Xu and G. Zeng, *Angew. Chem., Int. Ed.*, 2024, **63**, e202401750.

57 W. Li, B. Han, Y. Liu, J. Xu, H. He, G. Wang, J. Li, Y. Zhai, X. Zhu and Y. Zhu, *Angew. Chem., Int. Ed.*, 2025, **64**, e202421356.

58 T. Lu and F. Chen, *J. Comput. Chem.*, 2012, **33**, 580–592.

59 T. Lu, *J. Chem. Phys.*, 2024, **161**, 082503.

60 Z. Mi, T. Zhou, W. Weng, J. Unruangsri, K. Hu, W. Yang, C. Wang, K.-A. Zhang and J. Guo, *Angew. Chem., Int. Ed.*, 2021, **60**, 9642–9649.

61 Y. Qian, Y. Han, X. Zhang, G. Yang, G. Zhang and H.-L. Jiang, *Nat. Commun.*, 2023, **14**, 3083.

62 T. Le Bahers, C. Adamo and I. Ciofini, *J. Chem. Theory Comput.*, 2011, **7**, 2498–2506.

63 J. Yuan, Y. Yuan, X. Tian, Y. Liu and J. Sun, *J. Phys. Chem. C*, 2017, **121**, 8091–8108.

64 T. Yang, D. Zhang, A. Kong, Y. Zou, L. Yuan, C. Liu, S. Luo, G. Wei and C. Yu, *Angew. Chem., Int. Ed.*, 2024, **136**, e202404077.

65 H. Yan, Y. Huang, M. Shen, J. Xu, Y.-X. Ye and G. Ouyang, *Angew. Chem., Int. Ed.*, 2025, **64**, e202425054.

66 C. Chu, Z. Chen, D. Yao, X. Liu, M. Cai and S. Mao, *Angew. Chem., Int. Ed.*, 2024, **63**, e202317214.

67 W. Yu, F. Chen, X. Zhang, N. Tian, N. Zhang, Y. Zhang and H. Huang, *Nano Energy*, 2025, **138**, 110862.

68 J. Luo, X. Wei, Y. Qiao, C. Wu, L. Li, L. Chen and J. Shi, *Adv. Mater.*, 2023, **35**, 2210110.

69 C.-J. Wu, M.-Z. Shao, L.-J. Niu, T.-R. Li, W.-J. Liang, J.-L. Kan, Y. Geng and Y.-B. Dong, *Eur. J. Org Chem.*, 2023, **26**, e202300232.

70 Y. Zhao, K. Zhang, K. Zhu, Y. Zhao, H. Zhai and J. Qiu, *Green Chem.*, 2024, **26**, 2645–2652.

71 B. Kurpil, K. Otte, A. Mishchenko, P. Lamagni, W. Lipiński, N. Lock, M. Antonietti and A. Savateev, *Nat. Commun.*, 2019, **10**, 945.